



## 저작자표시-비영리-변경금지 2.0 대한민국

이용자는 아래의 조건을 따르는 경우에 한하여 자유롭게

- 이 저작물을 복제, 배포, 전송, 전시, 공연 및 방송할 수 있습니다.

다음과 같은 조건을 따라야 합니다:



저작자표시. 귀하는 원저작자를 표시하여야 합니다.



비영리. 귀하는 이 저작물을 영리 목적으로 이용할 수 없습니다.



변경금지. 귀하는 이 저작물을 개작, 변형 또는 가공할 수 없습니다.

- 귀하는, 이 저작물의 재이용이나 배포의 경우, 이 저작물에 적용된 이용허락조건을 명확하게 나타내어야 합니다.
- 저작권자로부터 별도의 허가를 받으면 이러한 조건들은 적용되지 않습니다.

저작권법에 따른 이용자의 권리는 위의 내용에 의하여 영향을 받지 않습니다.

이것은 [이용허락규약\(Legal Code\)](#)을 이해하기 쉽게 요약한 것입니다.

[Disclaimer](#)

**Master's Thesis**

**Dislocation Formation in Coaxial  
Heterostructural Nanotubes**

동축 이중 나노 튜브 구조에서의 전위 형성

**By**

**Aram Yoon**

**August 2012**

**Department of Materials Science and Engineering  
College of Engineering  
Seoul National University**

# **Dislocation Formation in Coaxial Heterostructural Nanotubes**

**Advisor : Prof. Miyoung Kim**

**By**

**Aram Yoon**

**A thesis submitted to the Graduate Faculty of Seoul National  
University in partial fulfillment of the requirements  
for the Degree of Master  
Department of Materials Science and Engineering**

**August 2012**

**Approved**

**By**

**Chairman of Advisory Committee : Young-Woon Kim**

**Vice-chairman of Advisory Committee : Young-Chang Joo**

**Advisory Committee : Miyoung Kim**

## Abstract

---

Here, we observed radially stretched dislocations making a 6-fold symmetric shape in a hexagonal nanotube of GaN/ZnO heterostructure. We investigated the effect of growth geometry of nanotubes on the formation of dislocations in one-dimensional heterostructure.

Formation of dislocation is mainly affected by strain field, i.e. strain from the mismatch of lattice parameters, and mismatch of thermal expansion coefficients, or thermal gradient. Despite a small lattice mismatch with ZnO and small thermal gradient, GaN still had high dislocation density. ZnO was used as a core shell template for heterostructure whose lattice mismatch with GaN is less than ~2%. Also, thermal gradients was less than 1 °C. Dislocation densities were locally different; the dislocation density was highest in the middle of the hexagonal facet, but no dislocation was observed at the corner (fig. 1). I analyzed the relation of geometry and dislocation's distribution from the aspect of strain field. First, the type of the dislocations and their Burgers vectors were identified by the large angle convergent beam electron diffraction (LACBED). LACBED method has an advantage of obtaining both an image of the specimen and the higher order Laue zone (HOLZ) lines simultaneously. The samples were tilted from the zone axis  $[\bar{1}011]$ . Burgers vectors were determined by ' $\mathbf{g} \cdot \mathbf{b} = n$ ' equation. The resulting Burgers vectors were mainly  $[\bar{1}120]$ , and dislocations had mostly edge character.

Second, local strain was analyzed by the convergent beam electron diffraction (CBED). Positions of HOLZ lines are very sensitive to local strains. Sample was tilted to an off-zone axis to avoid strong dynamic effects. The CBED images were taken from four different samples. At each corner and center of the hexagonal facet edge, several points were selected to examine the strain. Lattice parameters were determined by pattern matching with quantitative electron diffraction simulation and CBED images.

Finally, our experimental data was compared by a thermo-elastic finite element simulation considering the elastic anisotropy. The effect of thickness and geometry of nanotubes on strain gradient and dislocation generation was discussed.

---

**Key word:** Geometry induced dislocation, Convergent beam electron diffraction (CBED), Galium Nitride, heterostructure, Finite element method (FEM)

**Student number:** 2012-23190

**Aram Yoon**

# Contents

---

<b>Abstract.....</b>	<b>ii</b>
<b>Contents.....</b>	<b>iv</b>
<b>List of Figures.....</b>	<b>vi</b>
<b>1. Introduction.....</b>	<b>1</b>
<b>2. Literature survey.....</b>	<b>6</b>
2.1. Dislocation theory and strain source.....	6
2.1.1. Thermal stress and thermal dislocation .....	6
2.1.2. Misfit stress and misfit dislocation.....	7
2.2. Geometrically necessary dislocation.....	1 2
2.3. GaN and dislocation .....	1 4
2.3.1. Dislocation system in GaN thin film.....	1 4
2.3.2. Reduction of dislocation's densities.....	1 5
<b>3. Methods: Experiment and simulation.....</b>	<b>1 8</b>
3.1. Fabrication of GaN/ZnO nanotubes.....	1 8
3.2. Transmission electron microscopy .....	1 8

3.2.1.	Determination of burgers vector by LACBED.....	1 9
3.2.2.	Determination of lattice parameter and strain.....	2 1
3.3.	Simulations.....	2 5
3.3.1.	Dual-scale finite element modeling.....	2 7
<b>4.</b>	<b>Result.....</b>	<b>3 0</b>
4.1.	Burgers vector of dislocation.....	3 0
4.2.	Strain measurement.....	3 3
4.3.	Simulation.....	3 7
<b>5.</b>	<b>Conclusion.....</b>	<b>4 2</b>
<b>6.</b>	<b>국문 초록.....</b>	<b>4 3</b>
<b>7.</b>	<b>Reference.....</b>	<b>4 5</b>

## List of Figures

---

<b>Figure 1</b> (a) SEM image of nanotube array. TEM samples were prepared normal to the axis of nanotube. Bright field TEM image of nanotube (b) having full LED structure, (c) with high dislocation density, and (d) with low dislocation density. Dislocations were found mostly in the middle of the hexagonal facet .....	4
<b>Figure 2</b> Schematic structure of the nanotubes .....	5
<b>Figure 3</b> Time sequence illustrating misfit dislocation nucleation for a film with a positive (compressive) misfit of $f=+2.5\%$ <sup>31</sup> .....	9
<b>Figure 4</b> physical micromechanisms for relaxation of misfit stresses: (a) formation of a misfit dislocation row, and (b) formation of a misfit dislocation walls. $\lambda$ and $p$ are the sapcing between the walls and between the dislocations in a wall, respectively. <sup>32</sup> .....	1 1
<b>Figure 5</b> Schematic process(a-e) thorough which geometrically-necessary edge dislocation accumulate. <sup>35</sup> .....	1 3
<b>Figure 6</b> (a) Cross-section along the $[10\bar{1}0]$ zone axis of ELO film at the end of the first step. Dashed white lines join the dislocation bending points. (b) Schematic representation of film and dislocations. Dotted lines represent the shape of the ELO material at different stages of the first part of the ELO process. Dashed black lines join the successive edges of the top C facet. Continuous black lines represent dislocations. Schematic bending of the three basic edge dislocations with Burgers vector $b$ when they met the lateral facet <sup>39</sup> 1	7
<b>Figure 7</b> Cherns and Preston's rule. This rule enable us to determine	



burgers vector of dislocation. .... 2 0

**Figure 8** (a) Schematic image (left) indicates where the CBED patterns were taken and compared. Each position is called corner, and center. Whole CBED image was shown at the right hand side. The region marked with red box was cropped and presented below because HOLZ lines in that region were most sensitively moving. (b) CBED simulation patterns were obtained by JEMS simulation. Yellow dots and white arrows clarified the difference of each pattern. Differences were very clear in spite of small change in lattice constant. (c) Experimental CBED images were taken at bulk sample, corner, and center of the sample with a low density of dislocations..... 2 3

**Figure 9** parameters used for JEMS simulations using the Bloch wave approach..... 2 4

**Figure 10** Sapphire substrate, GaN buffer layer, SiO<sub>2</sub> film, and GaN/ZnO heterostructure compose the entire stacked system. Due to this vertical inhomogeneity, spatial changes in the system are inhomogeneous. (a) Deformation gradient profile at a specific region of interest (marked in the **Figure**) is generated from the upper-scale level simulation. In this step, detailed geometry of nanotubes is not considered because the principal direction of inhomogeneity is stacking direction. (b) Under assumption of the local periodicity, a representative volume element (RVE) can be specified. (c) The lower-scale level simulation considers detailed geometry of nanotube with rigorous periodic boundary condition ..... 2 6

**Figure 11** Material Properties for the dual-scaled analysis..... 2 9

**Figure 12** (a) Dark field TEM image.  $g=(11\bar{2}0)$  was excited, (b)

LACBED image on the dislocations. Dislocation pass thorough HOLZ lines of g vectors of  $(1451)$ ,  $(1896)$ ,  $(71140)$ ,  $(1123)$ , so that HOLZ lines spilt to several nodes. (c) Burgers vectors could be determined by counting spilt of HOLZ lines and setting up linear equations. .... 3 1

**Figure 13** CBED patterns were taken on the marked positions of 1(corner) and 2(center) in **Figure 1(c)**. (a) and (b) are raw data which were obtained corner and center respectively. For it is difficult to see the difference, lines were drawn as shown in **Figure (b)** and (e). **Figure (c)** and (f) are the images Hough-transformed from the **Figure (a)** and (d) to detect HOLZ line easily and to remove any prejudice. Arrows in (c) and (f) indicated movement of HOLZ lines, showing differently imposed strain field. .... 3 5

**Figure 14** Relative position where two HOLZ line meet (measured), and averaged lattice constant (fitted) ..... 3 6

**Figure 15** Calculated strain distribution of the representative GaN nanotube. (a) Tensile deformation is predicted at the bottom region (100 nm in height) of the nanotube. Compressive dominant deformation is evolved at the rest. (b) Cross-sectional image of 2000 nm position in height indicates almost uniform compressive strain distribution. (c) Whereas accumulated tensile deformation at the middle of hexagonal facet is shown in the cross-sectional image of 100 nm position in height. (d) Hoop directional strain profile indicates strong strain gradient along vertical. This strain gradient could act as a source of the geometrically necessary dislocation (GND). .... 3 8

**Figure 16** Calculated hoop strain distributions in the cross-sectional image of 100nm position in height for the cases under the consideration of (a) only the interface between the ZnO core and GaN shell and (b) only the interface between SiO<sub>2</sub> substrates and GaN nanotube (No ZnO layer)..... 4 0

# Introduction

---

Dislocations in nano-scale materials are critical to the properties and functionalities, especially when each of these materials is incorporated into nano devices. Here, we investigate the generation mechanism of crystal geometry-induced dislocations in GaN/ZnO hetero nanostructures. Dislocation types and local strain fields were determined by convergent beam electron diffraction method. We showed that the edge dislocation with burgers vector  $\frac{1}{3} [11\bar{2}0]$  released local residual strain fields created by lattice mismatches at two interfaces, between the substrate and hetero nanostructures as well as between ZnO core and GaN shell. Furthermore, we elucidate the relation between the nanostructure morphology and the highly localized dislocations based on the simulation by a finite element method. This work shows that the spatial distribution of geometry-dependent dislocations in nanostructures may be predicted, therefore, can be eluded by modifying the morphology of the structure.

Crystallographic defects, inevitably encountered in materials science, have long been studied because of their critical roles in mechanical, electrical, and optical properties. Moreover, defects and impurities have been intentionally incorporated to engineer physical properties in a range of device applications, and the role of defects in advanced technology is still evolving<sup>1-12</sup>. Dislocations in nanostructures, in particular, are of increasing interest because their contribution to the properties

becomes more significant as the size decreases, despite the fact that the dislocation density in a nanostructure is known to be very low because of the larger elastic strain accommodation and easy strain relaxation to the free side surfaces<sup>13, 14</sup>. Recently, hetero nanostructures which may have substantial misfit strain have attracted much attention because of the favorable architecture for monolithic nano devices, therefore, systematic study on strain induced dislocations in nanostructures is necessary.

Creation of misfit dislocations in a strained system is explained by the competition between elastic energies and dislocation formation energies. Indeed, finite element methods (FEM) have been applied for calculating strain fields in nano-heterostructures, including axial or core-shell heterostructures, in an attempt to find critical thickness or heights of dislocation-free nanostructures<sup>15-25</sup>. In nanostructured materials, information on not only the dislocation density but also spatial location of dislocations is essential for device operation, in particular for optical devices wherein optically active area should be defined. Here, we investigated the effect of crystal geometry in a nanoscale on the formation of dislocations in GaN, one of the leading materials for optoelectronics, grown as a GaN/ZnO coreshell tube structure on a SiO<sub>2</sub>/sapphire substrate (See **Figure 2** for schematics). Interestingly, in this nanostructure, misfit dislocations are localized in specific area with specific directions, as shown in transmission electron microscopy (TEM) images. (**Figure 1**) Locally confined dislocations made approximately a six fold symmetric shape in the

hexagonal GaN/ZnO nanotubes, and all dislocation lines have the equivalent crystallographic direction. In general, dislocations in GaN thin films, which often act as recombination centers in optical devices<sup>26-28</sup>, are known to be caused by relatively large lattice mismatch with available substrates; however, the localized dislocations in **Figure 1** cannot be explained simply by lattice mismatch only. Here, we measured strain fields by electron diffraction and used FEM for simulating spatial distribution of strain fields in nanostructures with different morphologies. This approach successfully elucidated the origin of the geometry-dependent dislocations in hetero nanostructures.

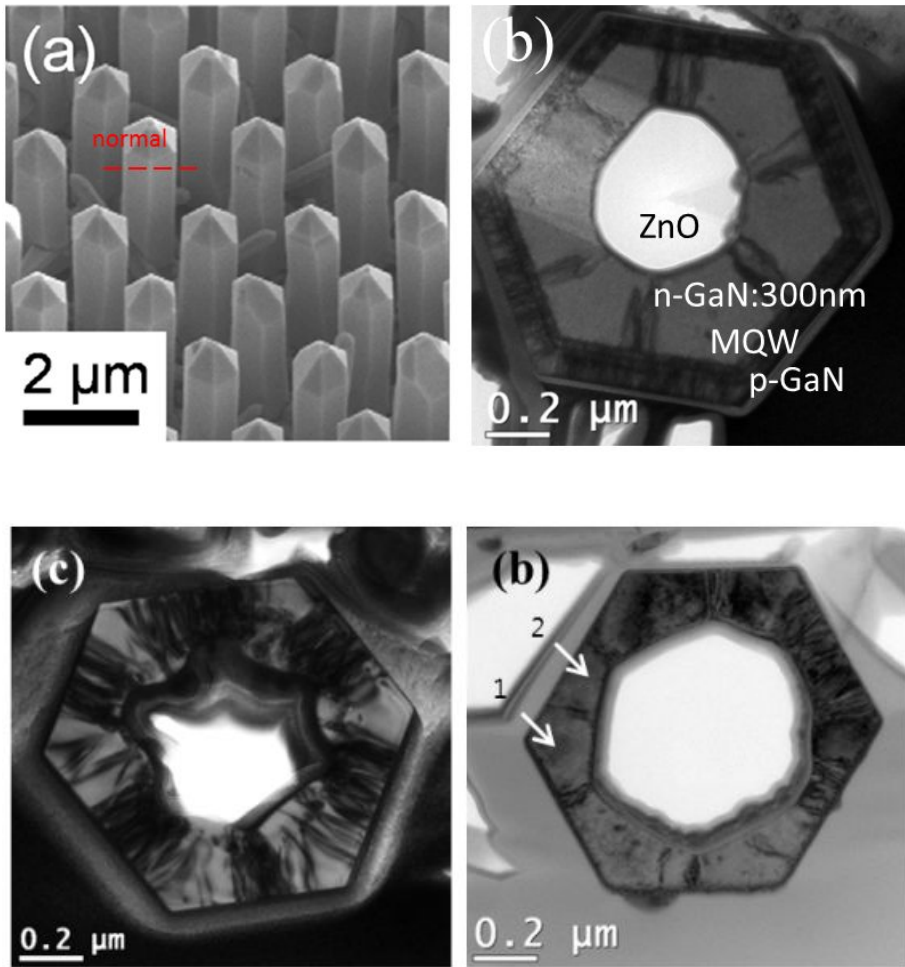


**Figure 1** (a) SEM image of nanotube array. TEM samples were prepared normal to the axis of nanotube. Bright field TEM image of nanotube (b) having full LED structure, (c) with high dislocation density, and (d) with low dislocation density. Dislocations were found mostly in the middle of the hexagonal facet

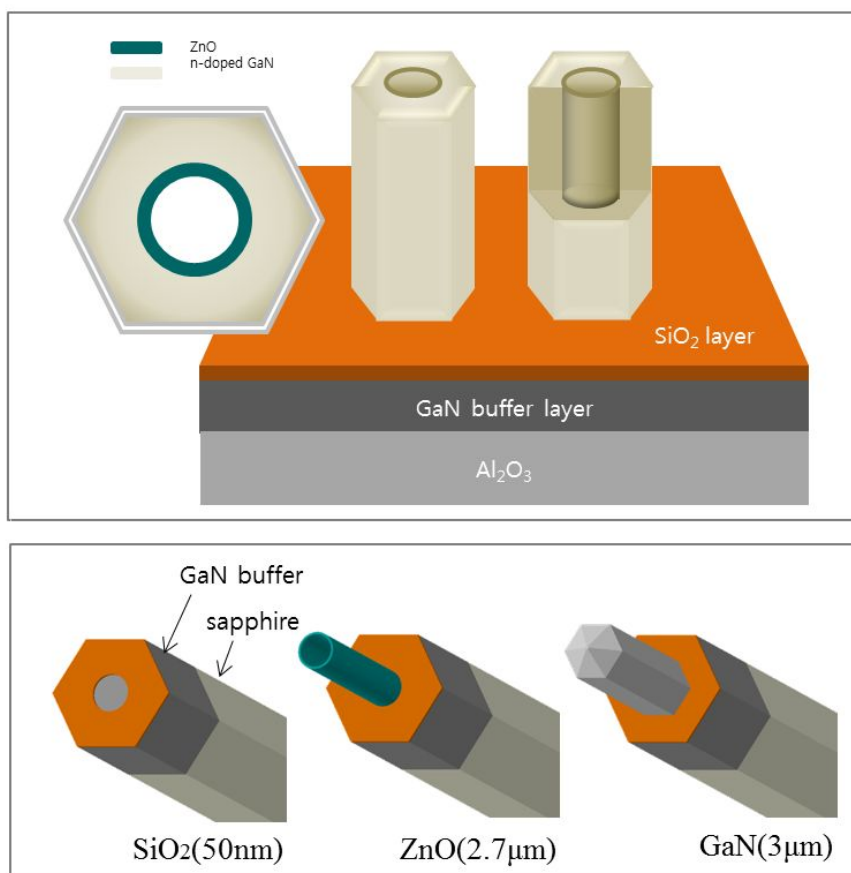


**Figure 2** Schematic structure of the nanotubes



## Literature survey

---

### 2.1. Dislocation theory and strain source

#### 2.1.1. Thermal stress and thermal dislocation

Thermal stress can be generated due to restrained thermal expansion/ contraction of temperature gradient that lead to differential dimensional change in different part of the solid body. It can be result in plastic deformation or fracture. In a rod with restrain, axial deformation is  $\sigma = E\alpha_l\Delta T$  where E is the elastic modulus,  $\alpha_l$  is the linear coefficient of thermal expansion and  $\Delta T$  is the temperature change.

Rapid heating can result in strong temperature gradient: confinement of expansion by colder parts of the sample. The same for cooling - tensile stresses are introduced in a surface region of rapidly cooled piece of material.

Thermal stresses can cause plastic deformation (in ductile materials) or fracture (in brittle materials). The ability of material to withstand thermal stresses due to the rapid cooling/heating is called thermal shock resistance. Shock resistance parameter for brittle materials (ceramics) is expressed as follows:  $TSR \propto \frac{\sigma_f k}{E\alpha_l}$  where  $\sigma_f$  is fracture strength of the material<sup>29</sup>.

By the residual thermal stress atoms can flow, and stress induced migration generates voids or other kinds of defects (disconnection, deformation, etc.). According to the stress-induced migration model, the formation process of voids

and disconnection due to stress-induced migration is considered to be as follows: vacancies generated thermodynamically in the metal interconnections migrate along the stress gradient, accumulate the vacancy sinks, and lead to the formation of voids and disconnection. Residual thermal stress can be relaxed by atomic migration forming dislocation or voids<sup>30</sup>.

### 2.1.2. Misfit stress and misfit dislocation

Misfit stresses occur in crystalline films due to the geometric mismatch at interphase boundaries between crystalline lattice of films and substrates. In most cases, a partial relaxation of misfit stresses is realized via a generation of misfit dislocations (MDs) that form dislocation rows in interphase boundary planes. One dimensional misfit characterized by the misfit parameter  $f = \frac{a_2 - a_1}{a_1}$  where  $a_1$  and  $a_2$  are the crystal lattice parameter of the substrate and the film, respectively.

Dong et al.<sup>31</sup> explain mechanism of the misfit dislocation's nucleation with a molecular dynamic simulation result. In case that mismatch of substrate and film is 2.5 % (compressive), the film develops a non-flat surface morphology prior to achieving the critical thickness (**Figure 3**). Because of compressive strain in the film, a highly compressive region develops at the bottom of the largest surface depression. In order to relax the high stress concentration at the bottom of the most prominent depression, the atoms adjust their positions and the plane of atoms at the bottom of the depression effectively buckles, ejecting an atom into the plane above it.

Removing this highly compressed atom in this way leaves the bottom of the surface depression in tension. Associated with this buckling event is the formation of an edge dislocation with a Burgers vector parallel to the substrate (oriented so as to relieve the misfit). To further relax the misfit strain, the dislocation climbs downward, toward the substrate, further relieving the strain.

In case of tensile stress (-5%) is different. misfit dislocations are formed by coordinated sliding events that produce two dislocations with Burgers vectors which are not parallel to the substrate, but which react to form a single dislocation with a Burgers vector oriented parallel to the substrate.

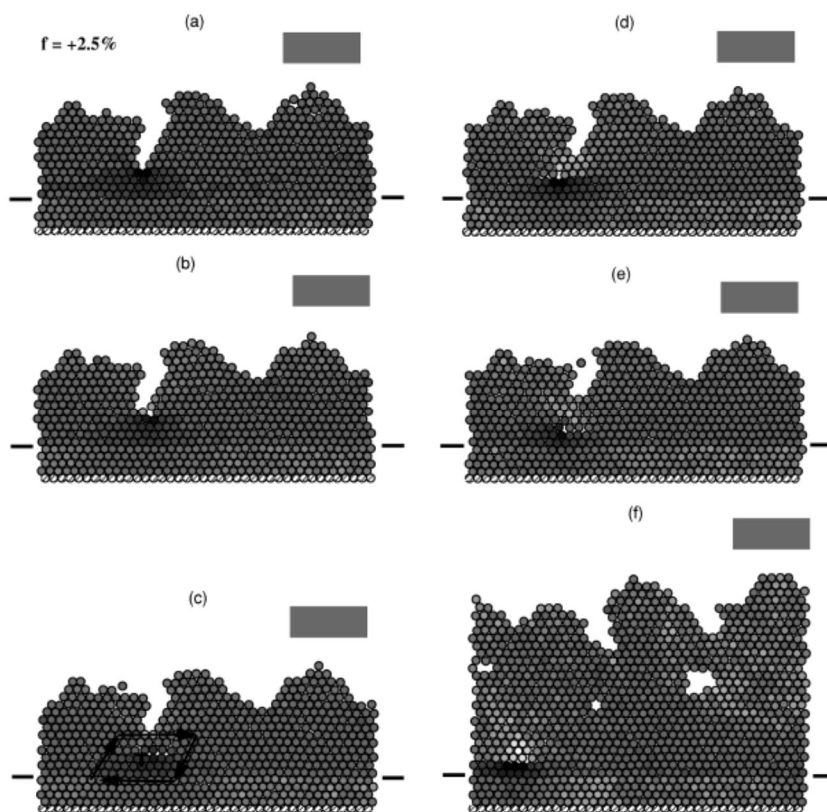


**Figure 3** Time sequence illustrating misfit dislocation nucleation for a film with a positive (compressive) misfit of  $f=+2.5\%$ <sup>31</sup>

Further, micromechanism for formation of misfit dislocation wall which is sequence of misfit dislocation above the interface rather a single dislocation has been investigated<sup>32</sup>(**Figure 4 (a)**). The standard physical micromechanism for relaxation of misfit stresses is the formation of array of misfit dislocations in the interphase boundary plane that induce compressive stress fields partly compensating for the tensile misfit stresses (or, in other words, partly accommodating misfit  $f$ ). However, they think that an effective alternative to the standard micromechanism is the formation of walls of misfit dislocations in the films that induce compressive stress fields (**Figure 4 (b)**). Whether it is the standard or the alternative micromechanism for relaxation of misfit stresses that is realized depends on kinetic factors (related to the technology of the deposition of the film on the substrate) and the degree of misfit stress relaxation caused by such micromechanisms. This suggests that formation of misfit dislocation walls is kinetically favorable depending on the growth condition at experiment regardless of the values of the ‘equilibrium’ parameters (critical thickness of a film, elastic energy density, etc) which characterize the walls.

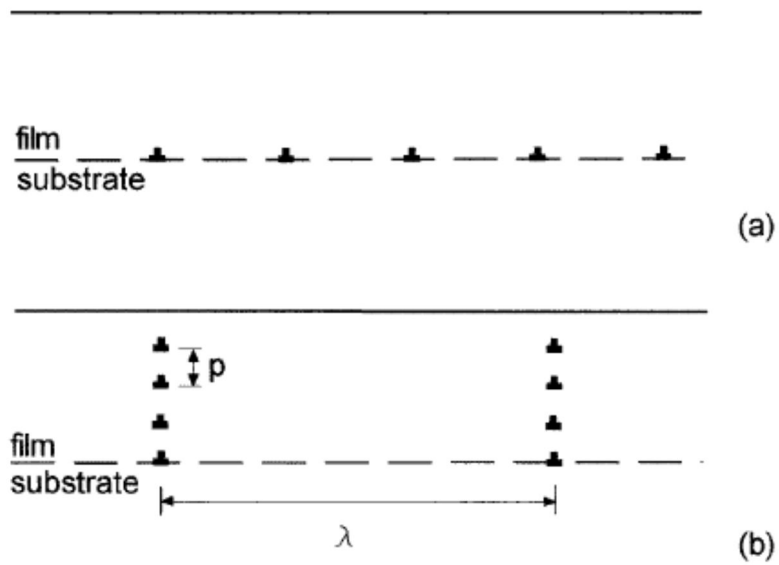


**Figure 4** physical micromechanisms for relaxation of misfit stresses: (a) formation of a misfit dislocation row, and (b) formation of a misfit dislocation walls.  $\lambda$  and  $p$  are the spacing between the walls and between the dislocations in a wall, respectively.<sup>32</sup>

## **2.2. Geometrically necessary dislocation**

Generally, material properties show size dependence at the sub-micron to micron level. Geometrically necessary dislocation first proposed by Nye<sup>33</sup> and furthered by Ashby<sup>34</sup> to explain material hardening increases as material's size decreases which classical theory had not accounted for: micro-indentation, bending experiment. All of these phenomena that stress size effect of material have associated with large strain gradient. This theory encloses strain gradient dependent material property. Geometrically necessary dislocations appeared in strain gradient field due to geometrical constrains of the crystal lattice (**Figure 5**)

Gradient in the plastic strain within crystalline materials give rise to dislocations in order to maintain continuity in the crystal. Furthermore, with knowledge of the crystalline orientation in relation needed to maintain lattice continuity is also specified. This theory is quite well adapted sub-micrometer sized material.<sup>35</sup>

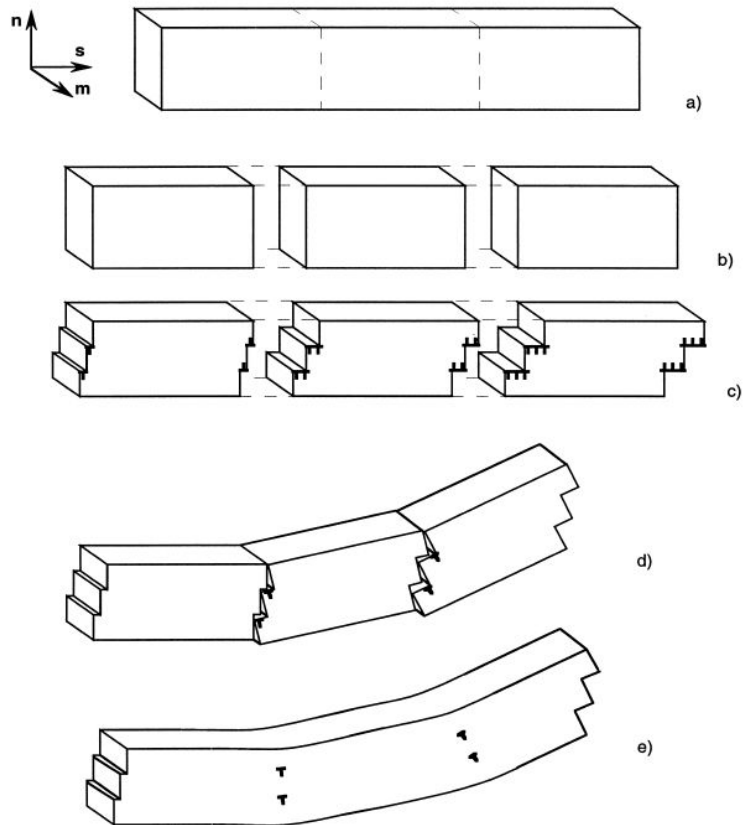


**Figure 5** Schematic process(a-e) thorough which geometrically-necessary edge dislocation accumulate.<sup>35</sup>



## 2.3. GaN and dislocation

Due to lattice mismatch and thermal expansion coefficient difference with the substrates, GaN films grown typically contain a large number of defects (mainly threading dislocation). The density of defects varies from  $1 \times 10^8$  to  $1 \times 10^{12}$  compared to  $10^4 \text{ cm}^{-2}$  found in arsenide and phosphide films. Extended defects such as dislocations and stacking faults are known to have a reduced effect on device operation in GaN, but at sufficiently high densities, threading dislocations adversely affect device properties.<sup>36</sup>

### 2.3.1. Dislocation system in GaN thin film

In case of GaN thin film grown on sapphire substrate, it is well known that there are primarily three types of threading dislocations in GaN films, each having one of the three Burgers vectors:  $\frac{1}{3} \langle \bar{1}1\bar{2}0 \rangle$ ,  $\langle 0001 \rangle$ ,  $\langle \bar{1}1\bar{2}3 \rangle$ . Most of the threading dislocations have their line vector of  $\mathbf{n}=[0001]$  when they start growing at the interface and dislocations dominantly have burgers vectors equivalent to  $\frac{1}{3}[\bar{2}1\bar{1}0]$ , which is edge character. GaN thin film exhibits a slip system of  $\{10\bar{1}0\} \langle \bar{2}1\bar{1}0 \rangle$ <sup>37</sup>.

On the other hand, a research reports that threading defects lysing on  $\{10\bar{1}0\}$  plane and bounded by opposite partial screw dislocations with Burgers vector of  $\frac{1}{2}\langle 0001 \rangle$  in single crystal c-oriented GaN nanorod grown on (0001) sapphire by molecular beam epitaxy. The faults nucleate, as dislocation half loops, from points close to the GaN/(0001) sapphire interface. It is proposed that the spiral growth of

the partial atomic step joining the emerging dislocations controls nanorod growth and accounts for the growth surface morphology<sup>38</sup>.

### **2.3.2. Reduction of dislocation's densities.<sup>1</sup>**

To reduce the density of dislocations, researchers use several method: hetero-epitaxy, epitaxial lateral overgrowth (ELO), and morphology control.

Since GaN bulk is not commercially available, heteroepitaxy with well matching substrate is essential. Whatever the heteroepitaxy, it usually requires several steps including nitridation of the substrate and/or deposition of a low temperature buffer layer and heat treatment of this nucleation layer. Since currently available substrate (sapphire or 6H-SiC) and GaN are highly mismatched, direct growth of GaN is impossible. Therefore, the growth of GaN on any substrate first requires the deposition of a buffer layer, which, to some extent, accommodates the mismatch. Using appropriate nucleation layers allows a reduction of the dislocation density to the low  $10^8 \text{ cm}^{-2}$  range.

In ELO technology, parts of the highly dislocated starting GaN are masked with a dielectric mask, after which growth is restarted. At the beginning of the second growth step, deposition only occurs within the openings, with no deposition observed on the mask. This is referred to as selective area epitaxy. The threading disllsocations are prevented from propagating into the overlayer by the dielectric

---

<sup>1</sup> Contents in this chapter were extracted from the review paper reference 39.

mask, whereas GaN grown above the opening (coherent growth) keeps the same threading dislocation's density as the template, at least during the early stages of growth<sup>39</sup>.

Of many structure, pyramidal GaN have reported few dislocation showing the dislocation filtering effect owing to presence of free surface. It has been argued that a dislocation grown through a small pore will be subjected to image forces from the free surfaces imposed by the pore wall, thus enabling the possibility of dislocation rejection (**Figure 6**).

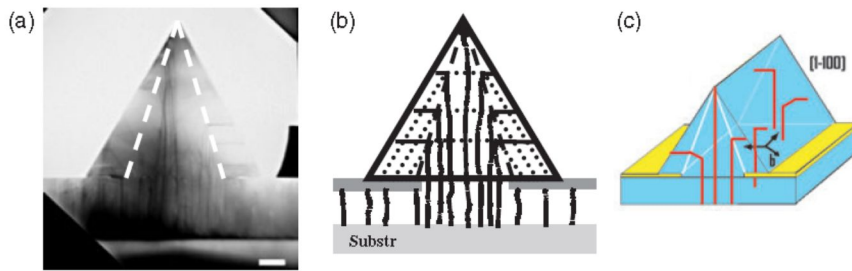


Figure 6 (a) Cross-section along the  $[10\bar{1}0]$  zone axis of ELO film at the end of the first step. Dashed white lines join the dislocation bending points. (b) Schematic representation of film and dislocations.

Dotted lines represent the shape of the ELO material at different stages of the first part of the ELO process. Dashed black lines join the successive edges of the top C facet. Continuous black lines represent dislocations. Schematic bending of the three basic edge dislocations with Burgers vector  $b$  when they meet the lateral facet<sup>39</sup>

# Methods: Experiment and simulation

---

## 3.1. Fabrication of GaN/ZnO nanotubes

The GaN/ZnO heterostructure nanotubes were grown by metal-organic chemical vapor deposition on sapphire substrates with a patterned silicon dioxide (SiO<sub>2</sub>) mask for the selective area growth. A GaN buffer layer was deposited on the sapphire substrate followed by a silicon oxide masking layer. Subsequently, the masking layer was patterned by lithography with diameters about 500 nm. ZnO nanotubes, whose thicknesses were estimated to several nanometers by SEM images, were selectively grown on the hole of the masking layer. N-doped GaN was layered on the ZnO template<sup>40</sup>. N-doped GaN thicknesses of the nanotube were between 100 nm and 200 nm and height of the nanotubes was all about 3  $\mu\text{m}$ . Schematics are in **Figure 2**.

## 3.2. Transmission electron microscopy

The cross-section specimens for TEM were prepared by focused ion beam, at the bottom and the top from each nanotube. Dislocation was analyzed by the TEM, Technai F20 operating at 200 KeV. For CEBD measurements, sample was tilted to an off-zone axis to avoid strong dynamic effects. Lattice parameters were determined by comparing quantitative electron diffraction simulation with CBED

images. Hough transformation was used to detect HOLZ lines from the experimental patterns<sup>41</sup>. The high tension of the microscope was determined first, then used for the refinement of the lattice constant,  $a$  and  $c$ .

### **3.2.1. Determination of burgers vector by LACBED**

Large angle convergent beam electron diffraction has advantages of obtaining both high order Laue zone lines and dislocation images at the same time. When dislocation lines cross the HOLZ line, HOLZ line splits to several lines. According to Cherns and Preston's rule, the Burgers vectors can be determined by counting HOLZ line splitting. LACBED disks were taken off and on the dislocations. HOLZ line that across the dislocation splits. By Cherns & Preston's rule<sup>42</sup> (See **Figure 7**), Burges vector is determined to be  $b=1/3[11-20]$ . This is known to be most stable<sup>43</sup> in hexagonal slip system

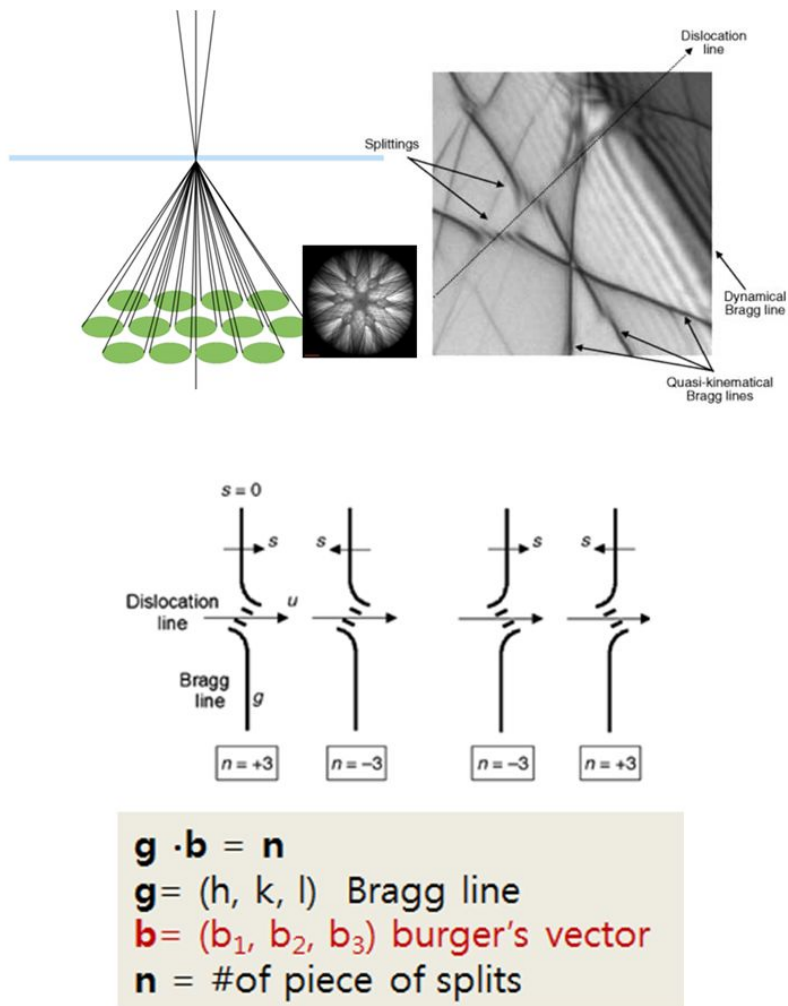


**Figure 7** Cherns and Preston's rule. This rule enable us to determine burgers vector of dislocation.

### 3.2.2. Determination of lattice parameter and strain

CBED was used to measure the lattice constant and strain fields. CBED images were obtained with a probe size of 10 nm and aperture of 10 micrometer size using Technai F-20. The high voltage of the microscope was calibrated using lattice constant of fully relaxed GaN films, in the range of micrometer thick. Several samples of GaN/ZnO nanotubes were examined with diversity of dislocation densities and nanostructure dimension. Mainly, two samples were compared: GaN/ZnO nanotube with a low density of dislocations, and GaN/ZnO nanotube with a high density of dislocations. Also, in a sample with a low density of dislocations, two parts of the hexagon were selected and compared: corner, and center. (See **Figure 8**)

HOLZ line simulations were performed using commercial program JEMS. Parameters used in JEMS simulation were indicated in **Figure 9**. Lattice constant a (and b)s were changed in between 3.190 Å and 3.196 Å. High tension voltage determined using bulk GaN was 199.3 KeV, by simulating known lattice parameter a of 3.190 Å. As lattice constant increased, the points indicated by white arrow were going up, the lower triangle got larger, Ratio of the lengths got smaller. At the corner, averages of lattice constants in GaN thin film, nanotubes with a few dislocations, and with a lot of dislocations were approximately close to 3.193 Å, slightly larger than that at bulk, it indicates that tensile strain field was residual in Both dislocation



densities. More importantly, increases from the corner to the center of the hexagonal facet in a sample with a few dislocations. Lattice constant was around 3.190 Å at corner while it was more closer to 3.196 Å at center. Measured values (ratio of length: upper length indicated to total length) were indicated in the **Figure 14**.

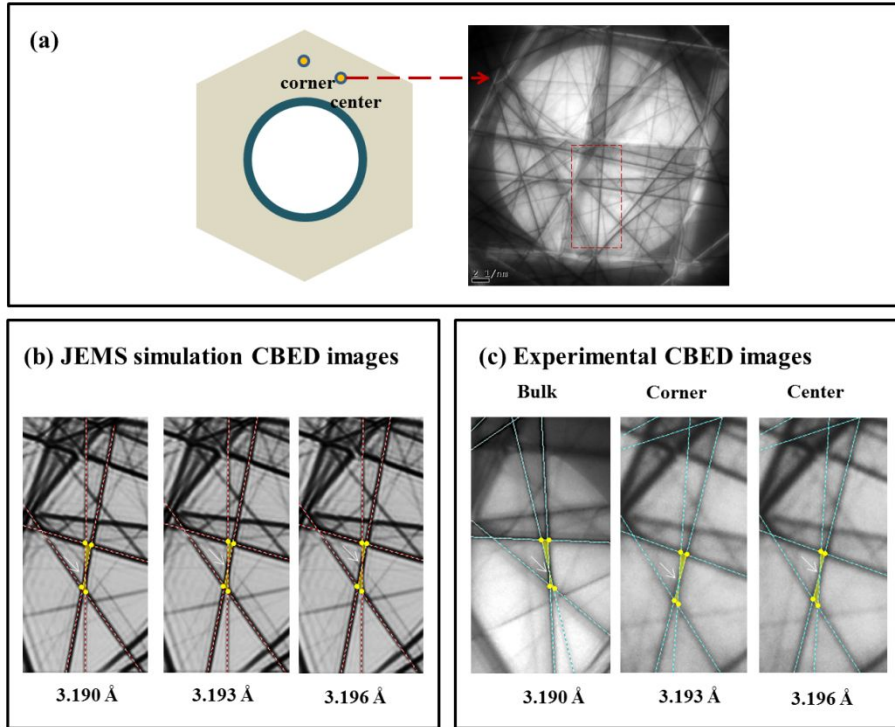


**Figure 8** (a) Schematic image (left) indicates where the CBED patterns were taken and compared. Each position is called corner, and center. Whole CBED image was shown at the right hand side. The region marked with red box was cropped and presented below because HOLZ lines in that region were most sensitively moving. (b) CBED simulation patterns were obtained by JEMS simulation. Yellow dots and white arrows clarified the difference of each pattern. Differences were very clear in spite of small change in lattice constant. (c) Experimental CBED images were taken at bulk sample, corner, and center of the sample with a low density of dislocations.

GaN crystal	
$\text{Ga}(\frac{2}{3}, \frac{2}{3}, 0), \text{Ga}(\frac{2}{3}, \frac{2}{3}, \frac{1}{2}), \text{N}(\frac{2}{3}, \frac{2}{3}, 0.3772), \text{N}(\frac{2}{3}, \frac{2}{3}, 0.8772)$	
Space group	P6 <sub>3</sub> mc
a	0.3180-0.3200 nm
c	0.5185 nm
$\alpha, \beta$	90°
$\gamma$	120°
Zone axis	[299, 85, 782]
Laue zone number	2
Acceptance angle	100 mrad
Camera length	9700 mm
Half-convergence angle	18.28 mrad
Voltage	200 kV
HOLZ threshold	435.0 mV
Specimen thickness	150 nm
Number of beams	330
Atomic form factors (PRDW) and D-W factors used were the default values given in JEMS	

**Figure 9** parameters used for JEMS simulations using the Bloch wave approach.

### 3.3. Simulations

A dual-scaled finite element modeling<sup>44</sup> was used for simulations. In a simulative view point, periodic systems like the GaN/ZnO heterostructure nanotubes have caused technical issues which are mainly associated with their infinite periodic nature. Since a single-scaled analysis over the entire system, of which calculating cost is quite high, is impractical, typical technique to deal with this type of structure is reduction of the entire system into a representative volume element (RVE). Given that the character of entire system is homogeneous during the process, this technique would be successful. However, the presented GaN/ZnO heterostructure should undergo inhomogeneous spatial change along vertical due to sequential stacking of films, leading the RVE concept inappropriate. Proposed dual-scaled scheme (**Figure 10**) is suitable technique for a tenuous periodic media, which originates from the inhomogeneity in periodic system.

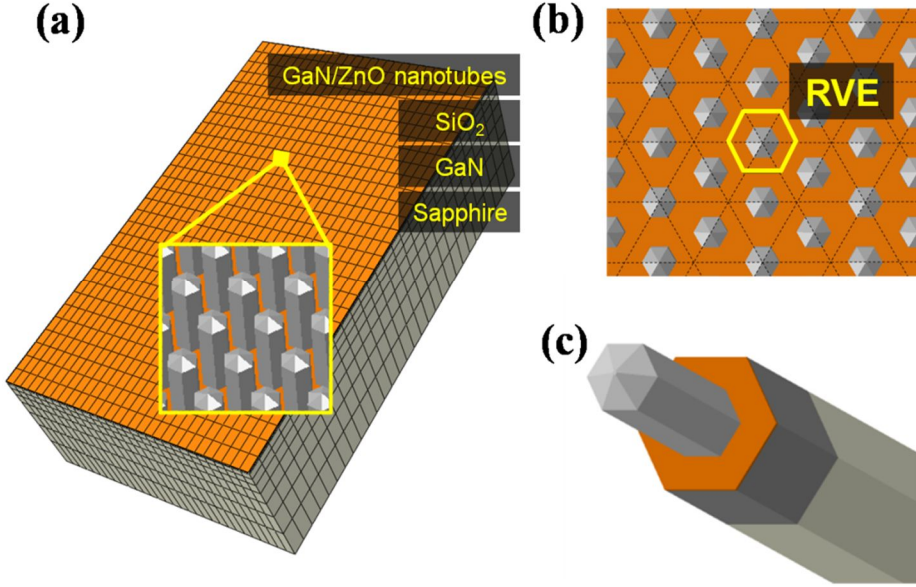


**Figure 10** Sapphire substrate, GaN buffer layer, SiO<sub>2</sub> film, and GaN/ZnO heterostructure compose the entire stacked system. Due to this vertical inhomogeneity, spatial changes in the system are inhomogeneous. (a) Deformation gradient profile at a specific region of interest (marked in the **Figure**) is generated from the upper-scale level simulation. In this step, detailed geometry of nanotubes is not considered because the principal direction of inhomogeneity is stacking direction. (b) Under assumption of the local periodicity, a representative volume element (RVE) can be specified. (c) The lower-scale level simulation considers detailed geometry of nanotube with rigorous periodic boundary condition

### 3.3.1. Dual-scale finite element modeling

Basic concept of the dual-scale analysis is a localized strong periodicity in a weakly periodic media. Each local region that includes hundreds or thousands of unit structure has relatively strong periodicity. This assumption leads a proper homogeneity for a specific local region. Therefore, progress of simulation is divided into two steps: (1) a preliminary simulation, so called upper-scalelevel analysis, to provide a deformation history of the local region of interest, and (2) lower-scale level analysis for a representative volume element (RVE) of that region.

The upper-scale level analysis is performed using homogenized elements which approximate complex periodic structure into a homogenized media. Thermo-elastic constitutive relation is considered with thermo-elastic anisotropy (**Figure. 11**). Strong inhomogeneity exists along stacking direction (**Figure. 10 (c)**), therefore the conventional technique using a single-scale RVE concept is inappropriate. Deformation history of the region of interest (marked in **Figure. 10 (b)**) is transferred to an ensuing simulation, lower-scale level analysis.

In the lower-scale level analysis, the boundary condition of periodic RVE subjected to the known deformation gradient,  $F$ , is<sup>45</sup>

$$u_B - u_A = (F - 1)(X_B - X_A) \quad (S1)$$

Where,  $u$ ,  $X$ , and  $I$  represent displacement, position, and identity tensor, respectively. Subscript A and B represent arbitrary two points located periodically on the

boundary of RVE. The deformation gradient,  $F$ , is set based on the results of the preliminary simulation described above.

Materials	Elastic Constants(GPa)					Coefficient of Thermal Expansion( $^{\circ}\text{C}^{-1}$ )		Lattice Parameter( $\text{\AA}$ )	
	C11	C12	C13	C33	C44	CTE(a-axis)	CTE(c-axis)	a	c
ZnO <sup>[b1][b2][b4]</sup>	184	93	77	206	56	$5.50 \times 10^{-6}$	$3.20 \times 10^{-6}$	3.24	5.2
GaN <sup>[b3][b4]</sup>	396	144	100	392	91	$4.10 \times 10^{-6}$	$3.00 \times 10^{-6}$	3.19	5.18
Al <sub>2</sub> O <sub>3</sub> <sup>[b5]</sup>	496	164	115	498	148	$1.05 \times 10^{-5}$	$9.77 \times 10^{-6}$	4.76	13.00

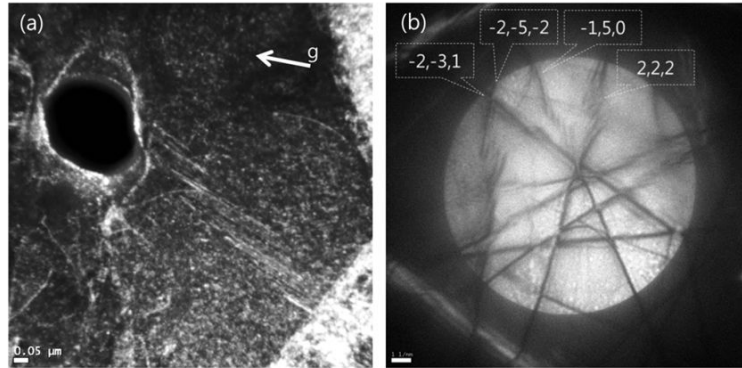
Material	Elastic Modulus(GPa)	Possion's ratio	CTE( $^{\circ}\text{C}^{-1}$ )	Expected atom distance( $\text{\AA}$ )
SiO <sub>2</sub> <sup>[b6][b7][b8]</sup>	75	0.17	$5.00 \times 10^{-7}$	5

**Figure 11** Material Properties for the dual-scaled analysis



### 4.1. Burgers vector of dislocation

To find the cause of the dislocation generation in this system, we determined the dislocation types and their Burgers vectors using the large angle convergent beam electron diffraction (LACBED) method and dark field images. LACBED method has an advantage of obtaining both an image of the specimen and the higher order Laue zone (HOLZ) lines simultaneously. The samples were tilted from the zone axis  $[\bar{2}111]$  (Figure 11). Burgers vectors were determined by Cherm's and Preston's rule<sup>29</sup>. Most dislocations had their dislocation line vector of equivalent  $n = [10\bar{1}0]$  and the resulting Burgers vectors were mainly  $b = 1/3[11\bar{2}0]$ , having edge type characters. These dislocations, which typically appear in the wurtzite lattice, are perfect and most energetically stable. Furthermore, it is beneficial for system to have such shape and position of dislocations in terms of dislocation energy, which is the lowest when its line is the shortest and magnitude of Burgers vector is the smallest.



(c) Tilting from the zone axis  $[-1\ 0\ 1\ 1]$

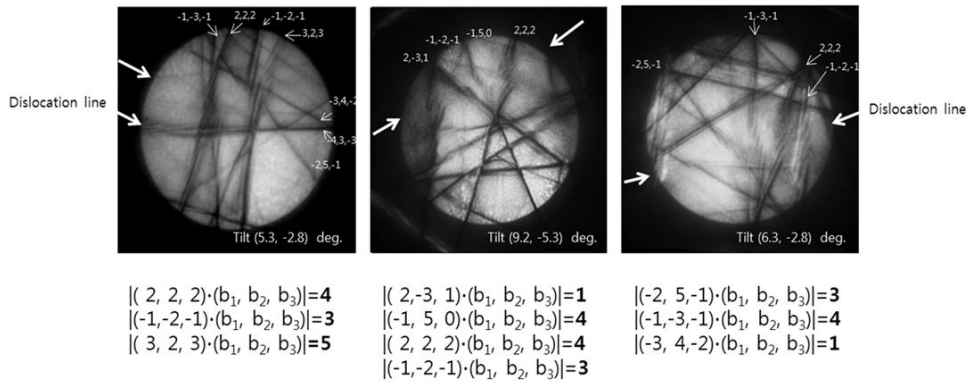


**Figure 12** (a) Dark field TEM image.  $g=(11\bar{2}0)$  was exited, (b) LACBED image on the dislocations. Dislocation pass thorough HOLZ lines of  $g$  vectors of  $(\bar{1}451)$ ,  $(\bar{1}896)$ ,  $(\bar{7}114\ 0)$ ,  $(11\bar{2}3)$ , so that HOLZ lines spilt to several nodes. (c) Burgers vectors could be determined by counting of HOLZ lines and setting up linear equations.

The edge type dislocations are usually created to release strain fields that arise from lattice mismatch in hetero-structure systems. In the present system, there are two possible interfaces which can generate strain fields; an interface between ZnO nanotube core and n-doped GaN, and between the substrate and the GaN/ZnO nanotubes. Another source of strain fields can be possibly the differences in thermal expansion coefficients or thermal gradients along the axial direction in the nanotubes when experimental growth condition is thermally in a non-steady state. Quantitatively, however, inhomogeneous temperature in the very small hetero nanostructure calculated by FEM was less than 1°C, thus the strain fields by thermal gradient cannot create the large number of dislocations observed.

The edge type dislocations with  $b = \frac{1}{3}[\bar{1}120]$  can release strain fields caused by lattice mismatch between ZnO and GaN, therefore, the interface could be a major reason for the generation of the dislocations in **Figure 1**. In this case, the dislocation lines in the hexagonal plane represent threading dislocations to the side surfaces. Maximum required number of edge dislocations that release the strain fields between ZnO and GaN is, however, much smaller than that appear in **Figure 1(c)**. There can be less than 10 dislocations in each area, considering the lattice misfit of about 1.5 % and the side length of 100 nm of hexagonal ZnO nanotube. It is also worth mentioning that many previous literatures also reported dislocation free nanostructures for low misfit core-shell system<sup>46, 47</sup>. In consequence, we can speculate the interface between the substrate and the nanostructures should be

additional major cause of the dislocation generation. Edge type dislocations with  $b=1/3[11\bar{2}0]$  can also accommodate strain field release at this interface.

## 4.2. Strain measurement

Although the lattice mismatch at these interfaces may provide enough stress to generate dislocations, this cannot explain the spatial distribution of highly localized dislocations. As noted earlier, dislocation energy proportional to the dislocation length may partially explain the localized dislocations at the center of hexagonal sides, which makes the line shortest. Additionally, convergent beam electron diffraction (CBED) method was used to examine the local residual strain. Position of HOLZ lines is very sensitive to lattice constants, and we used kinematic theory for the HOLZ line simulations. The structure for the simulation was maintained as a hexagonal structure with the same  $c$  parameter because the edge dislocations with  $b=1/3[11\bar{2}0]$  release strain in the hexagonal plane. Two kinds of GaN samples were prepared for comparative TEM study: One with high dislocation density (**Figure. 1(c)**) and the other with low dislocation density (**Figure. 1(d)**). **Figure 13** clearly show the shift of HOLZ lines obtained from two different positions marked as arrows in **Figure. 1(d)** in the GaN with low density of dislocations. Simulations show that lattice parameters at corner were close to the reported experimental value of  $a=3.190 \text{ \AA}$  and  $c= 5.18 \text{ \AA}$ , while  $a=3.196 \text{ \AA}$  in the middle of the hexagonal

facets, implying the presence of residual tensile strain. As we could have expected from the positions of the dislocations in the cross-sectional images, the strain was highest in the middle of the hexagonal facet when the strain was not completely released by enough misfit dislocations. In case of the samples with many dislocations there was little difference in the measured lattice constants at the center and the corner, similar to the one values of GaN with low density of dislocations. This implies that strain field was high at the nano-dimensional structures. These experimental results clearly indicate that strain fields generated by the lattice mismatches are not uniform in the hexagonal plane.

Lattice constants were statistically analyzed by examining several set of CBED patterns (See **Figure 14**). Lattice constants were statistically analyzed by examining several set of CBED patterns. Numbers in the tables are the relative position where certain two HOLZ lines meet. The measured ratio was inversely proportional to the lattice constant. Lattice constant were obtained by fitting these value to the simulation result by JEMS. Strain at the center of the hexagonal face is -0.1% relative at the corner. Both nanostructure with high and low density of dislocation

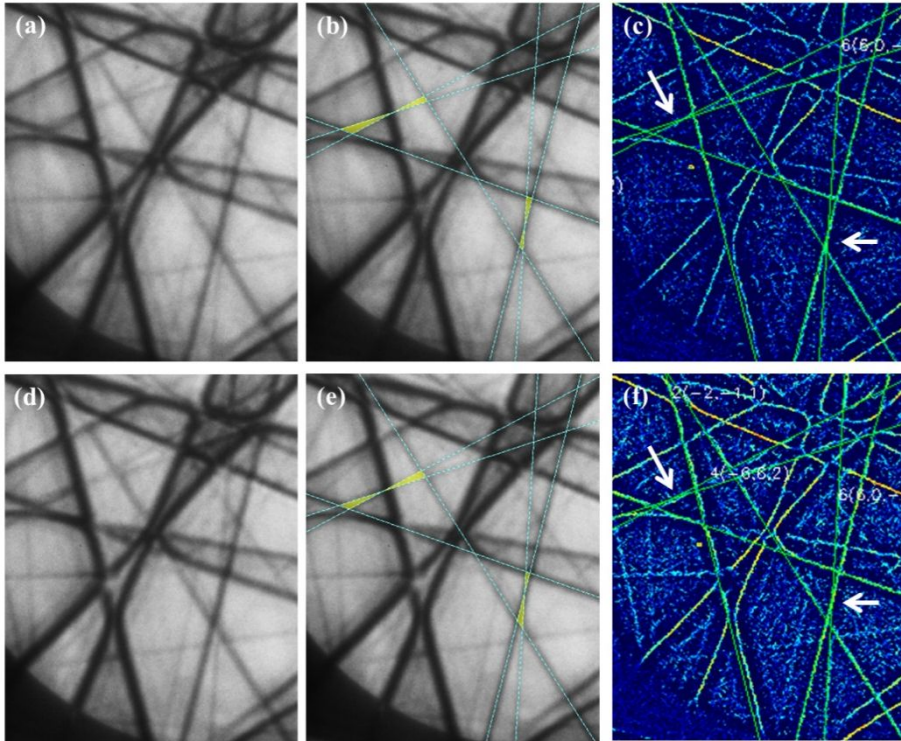


**Figure 13** CBED patterns were taken on the marked positions of 1(corner) and 2(center) in **Figure 1(c)**. (a) and (b) are raw data which were obtained corner and center respectively. For it is difficult to see the difference, lines were drawn as shown in **Figure (b)** and (e). **Figure (c)** and (f) are the images Hough-transformed from the **Figure (a)** and (d) to detect HOLZ line easily and to remove any prejudice. Arrows in (c) and (f) indicated movement of HOLZ lines, showing differently imposed strain field.

	<b>Bulk</b>	<b>High density</b>		<b>Low density</b>	
		corner	center	corner	Center
Average Ratio	0.669	0.556	x	0.584	0.450
Standard deviation	0.098	0.083	x	0.129	0.126
Average Lattice constant (Å)	3.190	3.193	x	3.192	3.196
Standard deviation	0.003	0.002	x	0.003	0.003

**Figure 14** Relative position where two HOLZ line meet (measured), and averaged lattice constant (fitted)

### 4.3. Simulation

The observed non-uniform strain fields were interpreted by a dual-scale finite element modeling, which can effectively handle the 3D infinite periodic heterostructure. Thermo-elastic constitutive relation considering the thermo-elastic anisotropy (**Figure. 11**) was used for the calculations. Temperature of the system was set to decrease from 1000°C to room temperature during crystal growth. With assistance from the dual-scale scheme, the calculation considers one of nanotubes as a representative volume element (RVE) for the entire system. This approach enables the prediction of spatial distribution of strain and stress in the GaN/ZnO heterostructure under the consideration of both its thermal and lattice mismatches.

Considerable misfit between crystalline GaN and amorphous SiO<sub>2</sub> could exist due to lattice mismatches<sup>48, 49</sup>. Ideally, this misfit strain is 0.6<sup>50</sup> (**Figure 15**), however amorphous Si atoms could be possibly rearranged to reduce the misfit. If the epitaxial ratio between crystalline GaN and amorphous SiO<sub>2</sub> is assumed to be 30%, the misfit strain is reduced to 0.1. Since the upper-scale level simulation does not take detailed geometry of nanotubes (including interface between GaN/SiO<sub>2</sub>) into account, we additionally consider this misfit in the lower-scale level simulation.



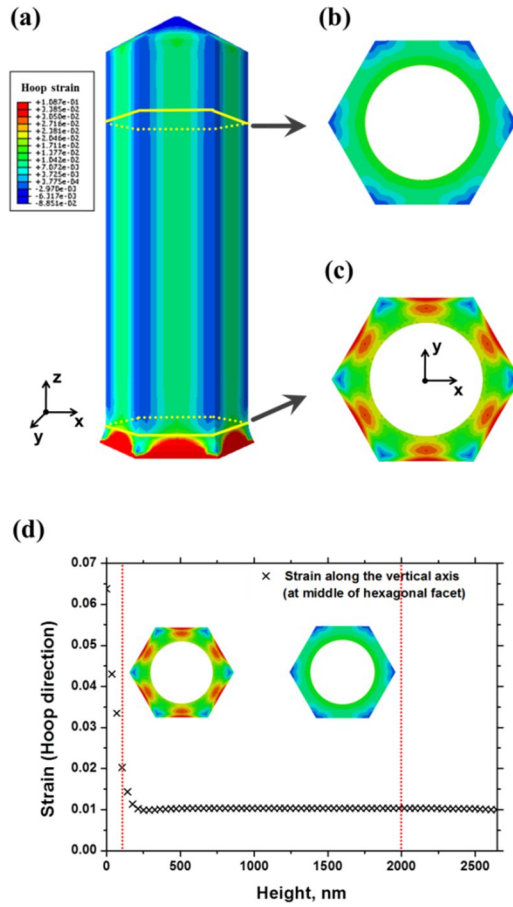


**Figure 15** Calculated strain distribution of the representative GaN nanotube. (a) Tensile deformation is predicted at the bottom region (100 nm in height) of the nanotube. Compressive dominant deformation is evolved at the rest. (b) Cross-sectional image of 2000 nm position in height indicates almost uniform compressive strain distribution. (c) Whereas accumulated tensile deformation at the middle of hexagonal facet is shown in the cross-sectional image of 100 nm position in height. (d) Hoop directional strain profile indicates strong strain gradient along vertical. This strain gradient could act as a source of the geometrically necessary dislocation (GND).

First, we calculated strain fields in the hexagonal plane generated by both interfaces, the interface between the substrate and nanostructures and between ZnO core tube and GaN shell. The simulation results show the representative nanotube bears inhomogeneous deformation during crystal growth (see **Figure. 15 (a)**), by the lattice mismatches between GaN nanotube and SiO<sub>2</sub> film<sup>48,49</sup>. Interestingly, the hoop strain was concentrated at the middle of hexagonal facet on the cross sectional plane in the nanotube (**Figure. 15 (b) and (c)**), consistent with the experimental CBED observations. In addition, bottom of the nanotube, which is connected to the film, is strongly elongated along hoop direction of the tube, whereas the rest is slightly tensioned. This inhomogeneity generates a strong strain gradient along the vertical direction of the middle of hexagonal facet (**Figure 15 (d)**). Under the strong strain gradient along vertical direction, atoms should flow down to the bottom, which are under tensile stress state, to fill the extra space caused by the tensile strain. This flow results in sequential extra half planes, or in other words, dislocations, which have edge characteristics. Accordingly, dislocations are bound to be the edge dislocation with burgers vector  $1/3 [11\bar{2}0]$  and prefer a center site of hexagonal facet. As a result, a concept of the geometrically necessary dislocation (GND)<sup>33,34</sup>, which appears in strain gradient fields due to geometrical constraints, can successfully explain the presence of accumulated dislocations at the middle of hexagonal facet. The differences in dislocation density could be explained by the growth conditions, such as mobility of amorphous SiO<sub>2</sub> at the high temperature<sup>51</sup> and the contact between

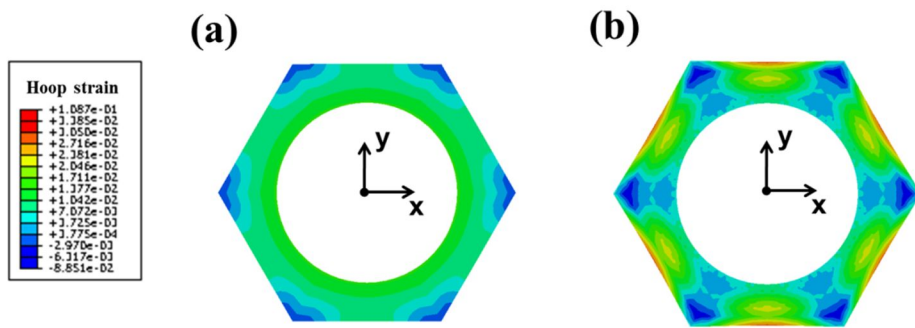


**Figure 16** Calculated hoop strain distributions in the cross-sectional image of 100nm position in height for the cases under the consideration of (a) only the interface between the ZnO core and GaN shell and (b) only the interface between SiO<sub>2</sub> substrates and GaN nanotube (No ZnO layer).

the amorphous substrate and the nanotubes.

It is much more interesting when we separate each interface effects by including only one interface in the simulations. Simulated strain fields by the interface between the ZnO core and GaN shell structure (**Figure. 15**) is similar to the **Figure. 16**, in the sense that strain is highest in the middle of the hexagonal facets although the range is much broader. This could be expected because the interface is in the hexagonal plane and GaN radius is expanding. **Figure 16** shows more localized strain fields which were generated by SiO<sub>2</sub> substrates and GaN nanotube (no ZnO layer) only, despite the fact that the interface is parallel to the hexagonal plane in this case. These results lead to the conclusion that the non-homogeneous strain fields are greatly enhanced in the presence of the interface effects between the substrate and the nanostructures, contributing to generate highly localized dislocations as shown in **Figure 1**. The same approach was repeated with GaN nanorod on SiO<sub>2</sub>, which show relatively homogeneous strain fields.

## Conclusion

---

In conclusion, we investigated the relation between misfit dislocations and crystal shape by examining highly localized symmetric dislocations of  $[10\bar{1}0]$  direction in the GaN/ZnO nanotubes. The dislocations were mostly edge dislocation with Burgers vector of  $1/3[11\bar{2}0]$ , originating from geometry of the nanostructure in the presence of stress at the interface. Furthermore, it is beneficial for system to have such shape and position of dislocation in terms of dislocation energy, which is the lowest when its line is the shortest and magnitude of Burgers vector is the smallest. In the nanotube hexagonal structure, lattice was pulled outward along the  $(11\bar{2}0)$  direction and easy to be under tensile strain. These evolve strain field and strain gradient along the vertical direction, which was effectively relaxed strain by introducing the dislocations at the position where the strain was the greatest.

## 국문 초록

---

나노 물질에서의 전위 생성은 벌크에 비해 억제된다고 알려져 있지만, 그럼에도 불구하고 소자의 작은 크기로 인해 적은 개수의 전위도 나노 소자의 구동에 크게 영향을 미칠 수 있다. 따라서 전위로 인한 문제들을 해결하기 위해 전위의 생성 원인과 효과, 그리고 전위 생성 억제 방법에 관한 많은 연구들이 진행되어 왔다. 전위를 일으키는 스트레인도 이중 구조의 격자 상수 차이가 유발하는 스트레인과 성장 과정에서의 열적 성질 차이에 의한 스트레인으로 구분한다. 전위 밀도와 형태는 이러한 스트레인이 어떻게 해소되느냐에 따라 결정되는데, 본 연구에서는 그 중에서도 격자 상수의 차이에 의해 생긴 스트레인이 나노 구조물의 형태에 따라 고르지 않게 분포하고 이를 효과적으로 해소하기 위해 서로 다른 밀도의 디스로케이션이 생성됨을 밝혔다.

광학 소자 재료의 하나로서 최근 활발히 연구되고 있는 GaN를 ZnO와 중심-겹질 형태의 이중 나노 튜브 형태 구조물로 만들었을 때 전위가 특정 방향으로 높은 전위 밀도로 생성되는 것이 관찰되었다. GaN은 wurzite 구조를 갖는 물질로서, 0001 방향으로 성장시킬 경우 육각형의 그레인 또는 나노 구조물의 형태를 갖는다. 이 때 전위는 주로 육각면의 중심 방향으로만 생성되고, 육각면의 꼭지점 방향으로서는 전위 밀도가 매우 낮았다.

이러한 전위의 분포를 투과전자 현미경으로 분석한 결과, 대부분  $1/2\langle 11\bar{2}0 \rangle$

20>의 버거스 방향을 갖는 칼날 전위였다. 스트레인의 분포를 수렴각 회절빔을 이용해 관찰한 결과 육각형의 중심과 모서리에서 스트레인 분포가 차이가 났으며 모서리보다 중심에 인장응력이 남아있었다. 이는 시편의 이중접합으로 인해 발생한 스트레인이 구조물 내에서 서로 다르게 분포할 수 있음을 보여주며, 유한 요소법을 통해 이를 뒷받침하는 결과를 얻었다. 더 나아가 유한 요소법을 이용해 스트레인을 줄 수 있는 변인을 통제 해 보면 나노 로드가 기판과의 접합이 강해질수록 스트레인이 육각면의 중심에 집중되는 효과가 더욱 컸다. 이로부터 전위의 생성이 나노 물질의 형태에 영향을 받는다는 것을 밝혀졌으며, 이를 역으로 이용하면, 나노 물질의 형태를 제어함으로써 전위의 생성과 분포를 제어할 수 있다는 결론을 얻는다.

---

**주요어:** 수렴빔 전자회절, GaN, 유한요소법, 도형유도전위, 이중접합물

**학 번:** 2012-23190

**이 름:** 윤아람

## Reference

---

1. Tuller, H. L. *Electrochimica Acta* **2003**, 48, (20-22), 2879-2887.
2. Bera, A.; Basak, D. *Applied Physics Letters* **2009**, 94, (16), 163119-3.
3. Dutta, S.; Chattopadhyay, S.; Sarkar, A.; Chakrabarti, M.; Sanyal, D.; Jana, D. *Progress in Materials Science* **2009**, 54, (1), 89-136.
4. Smith, A. M.; Mohs, A. M.; Nie, S. *Nature nanotechnology* **2009**, 4, (1), 56-63.
5. Dinadayalane, T. C.; Murray, J. S.; Concha, M. C.; Politzer, P.; Leszczynski, J. *Journal of Chemical Theory and Computation* **2010**, 6, (4), 1351-1357.
6. Omari, M.; Gupta, A.; Kouklin, N. *Journal of Applied Physics* **2010**, 108, (2), 024315-5.
7. Beane, G. A.; Morfa, A. J.; Funston, A. M.; Mulvaney, P. *The Journal of Physical Chemistry C* **2011**, 116, (5), 3305-3310.
8. Kabiraj, D.; Ghosh, S. *Journal of Applied Physics* **2011**, 109, (3), 033701-033701-6.
9. Lawrence, N. J.; Brewer, J. R.; Wang, L.; Wu, T. S.; Wells-Kingsbury, J.; Ihrig, M. M.; Wang, G.; Soo, Y. L.; Mei, W. N.; Cheung, C. L. *Nano Lett* **2011**, 11, (7), 2666-71.
10. Sevik, C.; Sevinçli, H.; Cuniberti, G.; Çağın, T. *Nano Lett* **2011**, 11, (11), 4971-4977.



11. Gu, H.; Jiang, Y.; Yan, M. *Journal of Alloys and Compounds* **2012**, 521, (0), 90-94.
12. Jegert, G.; Popescu, D.; Lugli, P.; Häufel, M. J.; Weinreich, W.; Kersch, A. *Physical Review B* **2012**, 85, (4).
13. Nam, C. Y.; Jaroenapibal, P.; Tham, D.; Luzzi, D. E.; Evoy, S.; Fischer, J. E. *Nano Lett* **2006**, 6, (2), 153-8.
14. Khanikara, P.; Kumarb, A.; Subramaniam, A. *Advanced Materials Research* **2009**, 67, 33-38.
15. Ye, H.; Lu, P. F.; Yu, Z. Y.; Song, Y. X.; Wang, D. L.; Wang, S. M. *Nano Lett* **2009**, 9, (5), 1921-1925.
16. Oswald, J.; Wintersberger, E.; Bauer, G.; Belytschko, T. *International Journal for Numerical Methods in Engineering* **2011**, 85, (7), 920-938.
17. Liang, Z.; Colby, R.; Wildeson, I. H.; Ewoldt, D. A.; Sands, T. D.; Stach, E. A.; García, R. E. *Journal of Applied Physics* **2010**, 108, (7), 074313.
18. Khanikar, P.; Subramaniam, A. *Journal of Nano Research* **2010**, 10, 93-103.
19. Colby, R.; Liang, Z.; Wildeson, I. H.; Ewoldt, D. A.; Sands, T. D.; Garcia, R. E.; Stach, E. A. *Nano Lett* **2010**, 10, (5), 1568-73.
20. Oswald, J.; Gracie, R.; Khare, R.; Belytschko, T. *Computer Methods in Applied Mechanics and Engineering* **2009**, 198, (21–26), 1872-1886.
21. Han, Y.; Pengfei, L.; Zhongyuan, Y.; Lihong, H. *Semiconductor Science and Technology* **2009**, 24, (2), 025029.

22. Zhao, W.; LaiWanga; JiayingWang; ZhibiaoHao; YiLuo. *Journal of Crystal Growth* **2011**, 327, 3.
23. Ertekin, E.; Greaney, P. A.; Chrzan, D. C.; Sands, T. D. *Journal of Applied Physics* **2005**, 97, (11), 114325-10.
24. Ye, W.; Paliwal, B.; Goh, W. H.; Cherkaoui, M.; Ougazzaden, A. *Computational Materials Science* **2012**, 58, (0), 154-161.
25. Raychaudhuri, S.; Yu, E. T. *Journal of Applied Physics* **2006**, 99, (11), 114308.
26. Karpov, S. Y.; Makarov, Y. N. *Applied Physics Letters* **2002**, 81, (25), 4721-4723.
27. Schubert, M. F.; Chhajed, S.; Kim, J. K.; Schubert, E. F.; Koleske, D. D.; Crawford, M. H.; Lee, S. R.; Fischer, A. J.; Thaler, G.; Banas, M. A. *Applied Physics Letters* **2007**, 91, (23), 231114.
28. Sugiura, L. *Journal of Applied Physics* **1997**, 81, (4), 1633-1638.
29. Shackelford, J. F., Introduction to Materials Science for Engineers. In 7 ed.; Prentice Hall: 2008; p 600.
30. Aoyagi, M. *Journal of Materials Research* **2011**, 19, (08), 2349-2355.
31. Dong, L.; Schnitker, J.; Smith, R. W.; Srolovitz, D. J. *Journal of Applied Physics* **1998**, 83, (1), 217.
32. Ovid'ko, I. A. *Journal of Physics: Condensed Matter* **1999**, 11, 6521-6527.
33. Nye, J. F. *Acta Metallurgica* **1953**, 1, (2), 153-162.
34. Ashby, M. F. *Philosophical Magazine* **1970**, 21, (170), 399-424.

35. Arsenlis, A.; Parks, D. M. *Acta Materialia* **1999**, 47, (5), 1597-1611.
36. Mathis, S. K.; Romanov, A. E.; Chen, L. F.; Beltz, G. E.; Pompe, W.; Speck, J. S. *Phys Status Solidi A* **2000**, 179, (1), 125-145.
37. Srinivasan, S.; Geng, L.; Liu, R.; Ponce, F. A.; Narukawa, Y.; Tanaka, S. *Applied Physics Letters* **2003**, 83, (25), 5187.
38. Cui, Y.; Li, L. *Physical Review B* **2002**, 66, (15).
39. Gibart, P. *Reports on Progress in Physics* **2004**, 67, (5), 667-715.
40. Hong, Y. J.; Jeon, J. M.; Kim, M.; Jeon, S. R.; Park, K. H.; Yi, G. C. *New Journal of Physics* **2009**, 11, (12), 125021.
41. Zuo, J. M.; Kim, M.; Holmestad, R. *Journal of Electron Microscopy* **1998**, 47, (2), 121-127.
42. Cherns, D.; Preston, A. R. *Journal of electron microscopy technique* **1989**, 13, (2), 111-22.
43. Flory, C. A.; Hasnain, G. *Ieee J Quantum Elect* **2001**, 37, (2), 244-253.
44. Cho, Y.-G.; Ahn, T.-H.; Cho, H.-H.; Moon, J. H.; Yang, S.; Han, H. N.; Li, J. *Acta Materialia* **2012(submitted)**.
45. Danielsson, M.; Parks, D. M.; Boyce, M. C. *Journal of the Mechanics and Physics of Solids* **2002**, 50, (2), 351-379.
46. Qian, F.; Gradecak, S.; Li, Y.; Wen, C. Y.; Lieber, C. M. *Nano Lett* **2005**, 5, (11), 2287-91.
47. Goldthorpe, I. A.; Marshall, A. F.; McIntyre, P. C. *Nano Lett* **2009**, 9, (11),

3715-9.

48. Jain, S. C.; Harker, A. H.; Cowley, R. A. *Philos Mag A* **1997**, 75, (6), 1461-1515.

49. Gao, H. J.; Zhang, L.; Baker, S. P. *Journal of the Mechanics and Physics of Solids* **2002**, 50, (10), 2169-2202.

50. Wriedt, B. H. A. *Bulletin of Alloy Phase Diagrams* **1990**, 11, (1), 43-61.

51. Lamkin, M. A.; Riley, F. L.; Fordham, R. J. *Journal of the European Ceramic Society* **1992**, 10, (5), 34-367.